Petroleum Science 23 (2026) 1387–1401

Contents lists available at ScienceDirect

Petroleum Science

journal homepage: www.keaipublishing.com/en/journals/petroleum-science

Original Paper

Synergistic alginate chelation and semi-interpenetrating network for advanced wellbore stabilizing hydrogels

Zhao-Jie Wei [a,b], Ying-Long Duan [c,**], Mao-Sen Wang [d], Ying-Hui An [d], Wen-Jing Qin [d], Ming-Yi Guo [d,*]

[a] Great Bay Institute for Advanced Study, School of Advanced Engineering/Great Bay University, Dongguan, 523000, Guangdong, China
[b] Institute for Ocean Engineering, Shenzhen International Graduate School, Tsinghua University, Shenzhen, 518055, Guangdong, China
[c] No. 2 Exploration Institute of Geology and Mineral Resources of Qinghai Province, Xining, 810000, Qinghai, China
[d] College of Construction Engineering, Jilin University, Changchun, 130021, Jilin, China

ARTICLE INFO

Article history:
Received 10 August 2025
Received in revised form
16 November 2025
Accepted 16 November 2025
Available online 20 November 2025

Edited by Yan-Hua Sun

Keywords:
Wellbore stability
Biocompatible alginate hydrogel
Semi-interpenetrating polymer network
Ca^{2+} chelation
Tunable gelation kinetics
Plugging performance

ABSTRACT

In situ plugging hydrogels represent a promising strategy to combat wellbore instability in fractured formations. Despite their potential, they often fail due to unpredictable gelation kinetics and inadequate mechanical strength under downhole conditions. Here, we introduce an alginate-based hydrogel (Alg-gel) engineered with an acid-triggered, multi-crosslinking mechanism that constructs a biodegradable shield directly within fractures. This system integrates sodium alginate (SA) with hydroxypropyl guar gum (Hpg) to form a primary semi-interpenetrating network. The critical innovation lies in the synergistic use of D-gluconic acid δ-lactone (GDL) and $CaCO_3$, which enables precise, sustained release of Ca^{2+} ions. These ions subsequently coordinate with guluronate blocks in SA, establishing a secondary network that embeds residual $CaCO_3$ as reinforcing scaffolds. This multi-network architecture results in a storage modulus increase by orders of magnitude and reduces filtration loss by up to 89.3% as gelation proceeds from 30 to 180 min. Structural evolution from a sparse framework to a densely interlocked lamellar assembly was directly visualized, validating the tunable nature of the complexation process. The exceptional plugging performance and controllable gelation kinetics position Alg-gel as a superior lost circulation material, with broader implications for profile modification and gas channeling mitigation.

1. Introduction

Drilling serves as the fundamental conduit for accessing subsurface oil, gas, and geological resources, yet its efficiency is persistently compromised by lost circulation—a paramount technical and economic challenge in petroleum engineering. This phenomenon predominantly originates from natural formation porosity and, more critically, from the propagation of pressure-induced fractures. Subsequent wellbore instability events, including stuck pipe, borehole collapse, and blowouts, can increase operational time by over 70% (Bai et al., 2023). The financial burden is substantial, with mitigation costs reaching $70–100 per foot (Kibikas et al., 2024), which constitutes 10%–20% of total well expenditure (Lin et al., 2024).

Conventional practice to enhance wellbore stability employs solid plugging agents, such as calcium carbonate, rubber particles, nut shells, and asphalt, which are incorporated into drilling fluids. Within this approach, coarse-grade particulates function by bridging fracture throats, while fine-grade fillers subsequently pack the interstitial voids (Xu et al., 2023; Yan et al., 2024). Nevertheless, such physical packing materials are inherently limited by weak interparticle cohesion and insufficient sealing integrity. Consequently, they remain vulnerable to mechanical disturbances, including pressure surges and hydraulic scouring, which can displace the packed particles and substantially degrade the sealing capacity and pressure-bearing performance (Zang et al., 2025).

Preformed particle gels (PPGs) have emerged as promising sealing agents due to their superior plugging capacity and

* Corresponding author.
** Corresponding author.
E-mail addresses: 18097315128@163.com (Y.-L. Duan), guomingyi@jlu.edu.cn (M.-Y. Guo).

Peer review under the responsibility of China University of Petroleum (Beijing).

https://doi.org/10.1016/j.petsci.2025.11.030

transport properties. Expandable PPGs, fabricated from pre-crosslinked polymers or shape-memory composites, can undergo designed volumetric expansion upon thermal or aqueous activation downhole to seal fractures (Zhao et al., 2025a). However, the difficulty in precisely controlling their activation kinetics and achieving optimal size matching with dynamic fracture networks hinders their widespread application. Alternative strategies, such as cementitious systems and stimuli-responsive hydrogels, present their own trade-offs (Kang et al., 2024). While cement slurries provide robust sealing across a wide aperture range, their unpredictable setting behavior and poor removability pose significant risks of permanent formation damage (Cui et al., 2021; Mirabbasi et al., 2022). In situ polymerizing hydrogels, which gel via mechanisms like ring-opening polymerization (Liu et al., 2025a), or hydrophobic association (Pereira et al., 2022), offer excellent conformance to fracture geometry (Wang et al., 2023b). Nevertheless, their gelation kinetics and final performance are critically dependent on specific and uncertain reservoir conditions (e.g., temperature, ionic composition), making reliable deployment challenging. Consequently, a pressing need remains for a plugging material that combines controllable activation, self-adaptive sealing, and operational reliability under complex downhole environments (Bai et al., 2021; Sun et al., 2023a).

Acrylamide-based hydrogels represent a mainstream chemical solution for lost circulation control. These systems are typically fabricated through free-radical copolymerization of monomers such as acrylamide and 2-acrylamido-2-methylpropane sulfonic acid (Ma et al., 2024; Sun et al., 2023c), crosslinked by covalent agents (e.g., phenol-formaldehyde resins, polyethyleneimine) (Chen et al., 2024) or multivalent metal ions (e.g., Cr^{3+}, Fe^{3+}, and Zr^{4+}) (Bai et al., 2015). The resulting low-viscosity prepolymer solution is injected into the loss zone, where it undergoes a sol–gel transition in situ, forming a viscoelastic network that seals fractures via covalent bonding and ionic coordination (Guo et al., 2024a). Despite their effectiveness, these hydrogels face growing regulatory and environmental concerns over the toxicity of residual monomers and heavy metal crosslinkers (Bai et al., 2022a; Guo et al., 2024b). Consequently, the development of high-performance plugging materials that simultaneously achieve tunable gelation, robust pressure resistance, and full environmental compliance remains a critical unsolved challenge in field operations (Wu et al., 2024).

Natural polysaccharides (e.g., chitosan, alginate acid, carrageenan, and cellulose) have emerged as sustainable and versatile platforms for engineering in situ polymerized hydrogels (Pan et al., 2023; Shariatinia and Jalali, 2018; Su et al., 2023; Wu et al., 2022). These biopolymers combine abundant availability, intrinsic environmental compatibility, and versatile chemical functionality, enabling the creation of densely crosslinked networks with precisely tunable gelation dynamics and robust mechanical properties (Dai et al., 2025). Despite forming effective crosslinked networks, conventional hydrogels often exhibit limited fracture toughness and insufficient mechanical strength due to the absence of a rigid structural framework. This inherent brittleness can lead to premature failure under downhole stress, compromising both fracture retention and long-term sealing integrity. To overcome these limitations, rigid particulates are frequently incorporated into the gel matrix, where they function as reinforcing scaffolds that enhance network density through physical bridging and skeletal support. The resulting composite materials, rigid particle-reinforced hydrogels, thus represent a promising approach to establishing a synergistic physicochemical barrier that combines superior pressure-bearing capacity with enhanced retention stability (Hamza et al., 2020; Zhai et al., 2020).

Alginate acid, an anionic polysaccharide composed of β-D-mannuronic acid (M-block) and α-L-guluronic acid (G-block), has been widely employed in industrial and biomedical applications since the 1920s. Its sodium salt, sodium alginate (SA), is particularly valued for its gel-forming ability, biocompatibility, and sustainability (Liu et al., 2025b; Zhang et al., 2022), finding broad utility in food preservation (Ming et al., 2025; Xie, 2024), pharmaceuticals (ElTatawy et al., 2024; Zhao et al., 2025b), agriculture (Bakhshizadeh et al., 2022; Wang et al., 2023a), and energy systems (Gao et al., 2024; Ji et al., 2022). In drilling engineering, SA has been used to enhance fluid performance via adsorption onto bentonite surfaces (Wei et al., 2022), while potassium alginate (PA) has demonstrated effective shale inhibition through polymer film formation (Wei et al., 2024). More recently, SA-based self-healing preformed particle gels have been developed using hydrophobic copolymerization and Fe^{3+} coordination, showing promising fracture sealing performance (Bai et al., 2022c; Zhang et al., 2022). Nevertheless, the potential of SA to form in situ reinforced hydrogels through a combined strategy of polymer entanglement, ionic crosslinking, and rigid-particle scaffolding remains inadequately explored, particularly the synergistic interplay between these mechanisms.

Inspired by previous work on dual-network polysaccharide hydrogels and the recognized limitations of single-mode crosslinking systems, we first selected several biopolymer candidates, including hydroxypropyl guar gum (Hpg), curdlan (Cur), carboxymethyl chitosan (Cmcs), pregelatinized cassava starch (Pgcs), agar, and gelatin—for their ability to form entangled networks with SA. Among these, the hydrogen bonding interactions formed by the combination of SA and Hpg are particularly significant, forming a tight primary network. Herein, we develop an alginate-based hydrogel featuring a multi-network architecture for lost circulation control. The primary network is established through hydrogen bonding between SA and Hpg, while the hydrolysis of glucono-δ-lactone (GDL) gradually releases Ca^{2+} from $CaCO_3$, inducing a secondary “egg-box” coordination network. In this system, $CaCO_3$ particles act both as reservoirs of Ca^{2+} for ionic crosslinking and as rigid skeletons that provide structural reinforcement. Following formulation optimization for gelation kinetics and plugging efficiency, the multi-crosslinking mechanism was systematically elucidated by morphological analysis, FTIR characterization, real-time pH monitoring, and Ca^{2+} release profiling. Plugging performance and fracture adaptability were further validated in simulated porous formations with different pore structures. Owing to its high adaptability and sealing efficiency conferred by the multi-crosslinked architecture, the in situ SA-based hydrogel offers a promising high-performance alternative to conventional lost circulation materials (LCMs) in drilling operations, with potential extensions to fracturing fluids and sand consolidation.

2. Materials and methods

2.1. Materials

SA (viscosity: 200±20 mPa·s; M/G ratio: 1.0; $M_w = 8.7 \times 10^4$ Da; 99.7%) and D-gluconic acid δ-lactone (GDL, purity: $\geq$ 99%) were purchased from Aladdin Chemical Reagent Co., Ltd. (Shanghai, China). Pgcs (viscosity: 500±30 mPa·s; $M_w = 1.5 \times 10^5$ Da; purity $\geq$ 98%) was obtained from Senruite Biotechnology Co., Ltd. (Shandong, China). Hydroxypropyl guar gum (Hpg, viscosity: 1000±50 mPa·s; molar substitution = 1.6; $M_w = 2.0 \times 10^5$ Da; purity $\geq$ 98%) and Cur (viscosity: 30±1.5 mPa·s; $M_w = 4.0 \times 10^5$ Da; purity $\geq$ 98%) were supplied by Haiaosi Biotechnology Co., Ltd. (Shandong, China). The viscosity of Cur was determined in mildly

alkaline aqueous. Cmcs (viscosity: 60±3.0 mPa·s; $M_w = 2.4 \times 10^5$ Da; degree of carboxylation ≥ 85.0%), gelatin (type A, derived from porcine skin; $M_w = 8.9 \times 10^4$ Da; gel strength: 250 Bloom), and agar (gel strength: 1500 g/cm^2; $M_w = 4.3 \times 10^5$ Da; moisture content ≤ 10%; gelling temperature: 41.2 °C; sulfate content: 0.47%) were purchased from Sigma-Aldrich (Shanghai, China). All materials were powders, readily water-soluble, and used without further purification. The viscosity was measured using a Brookfield LV viscometer (Model DV2, USA) at 25 °C with a polymer concentration of 1.0 wt%. Unless stated otherwise, compositional and molecular parameters were sourced from supplier analytical certificates.

Calcium lactate (CL, ≥ 98%), calcium chloride ($CaCl_2$, ≥ 97%), and Eriochrome Black T (EBT, Ca^{2+} indicator) were obtained from Macklin Reagent Co., Ltd. (Shanghai, China). Calcium carbonate ($CaCO_3$, 95%) with a range of particle sizes (1250, 1000, 800, 600, 375, 200, and 100 mesh) was purchased from Lingshou Mining Processing Products (Hebei, China). Shale, basalt, and gravel cuttings were collected from a drilling site in the Songliao Basin, China, and were oven-dried and crushed prior to use.

2.2. Methods

2.2.1. Preparation of Alg-gel

Alg-gel was prepared via acid-triggered in situ gelation by introducing GDL solution into a polymer suspension containing $CaCO_3$ (Fig. 1). Briefly, 2.4 g of polymer (SA, Ppcs, Hpg, Cur, Cmcs, gel, or agar) was dissolved in 300 mL deionized water at 25 °C under constant stirring using a GJS-B12K overhead stirrer (Tianjin Hengxing Chemical Reagent Manufacturing Co., Ltd., China) at 1000 rpm for 30 min. The solution was then sealed and hydrated for 12 h at ambient temperature. Next, 12 g of calcium source ($CaCO_3$, $CaCl_2$, or CL) was added and dispersed into the polymer solution at 2000 rpm for 30 min. $CaCO_3$ with varying particle sizes (11.8–38.0 μm, ASTM standard) and concentrations (1.0–5.0 wt%) was employed to investigate their influence on gelation behavior. Detailed discussion of how particle size and dosage regulate Ca^{2+} release, gelation kinetics, and final performance is provided in the discussion section. Separately, GDL was dissolved in 100 mL deionized water and added to the suspension to initiate gelation. Real-time pH was monitored using a Seven Excellence S500-Basic pH meter (Mettler-Toledo, Switzerland), calibrated with pH 4.0 and 7.0. Free Ca^{2+} release was quantified at 30, 60, 90, 120, 150, and 180 min by classical EDTA titration with EBT as the indicator.

2.2.2. Characterization techniques

Alg-gel samples at designated gelation intervals were cut into 1 cm^3 cubes, rapidly frozen in liquid nitrogen, and lyophilized (freeze dryer ZLGJ-20, Huachen Instrument Co., Ltd., Zhengzhou, China) at −60 °C and 0.1 mbar for 48 h. The freeze-dried specimens were sputter-coated with gold for 150 s and examined by a scanning electron microscope (SEM, Hitachi S-4800, Tokyo, Japan) at an accelerating voltage of 10 kV to visualize the internal microstructure. For chemical characterization, dried hydrogel samples were finely ground and thoroughly mixed with potassium bromide (KBr) at a mass ratio of 1:100. The mixture was then compressed into transparent pellets and analyzed by Fourier transform infrared spectrometer (FTIR, Nicolet iS10, Thermo Scientific, USA) over 4000–450 cm^{-1} with a resolution of 4 cm^{-1}.

2.2.3. Rheological measurements

Rheological behavior of Alg-gel at various gelation stages was measured on a rotational rheometer (DHR-2, TA Instruments, Waters LLC, New Castle, DE, USA) equipped with a 40 mm parallel plate geometry and a fixed gap of 1.00 mm. Prior to testing, gels were rested at ambient conditions for 6 h to release entrapped air and allow structural stabilization. To identify the linear viscoelastic region (LVR), amplitude sweep tests were performed from 0.01% to 1000% at 1.0 Hz. Frequency sweep tests were then conducted within the LVR from 0.01 to 20.00 Hz to obtain the storage modulus (G') and loss modulus (G''). Each rheological measurement was repeated three times to ensure reproducibility. Additionally, qualitative gel strength was assessed by the Sydansk bottle test, in which gels were visually graded from A to G based on settling behavior (Song et al., 2023), as illustrated in Fig. 2.

2.2.4. Plugging performance tests

To evaluate the time-dependent plugging performance of Alg-gel in porous and fractured media, simulated formations with porosities of 35.7%, 46.3%, and 57.1% were prepared using shale, gravel, and basalt cuttings, respectively. A total of 300 cm^3 of dried and sieved cuttings were uniformly packed into a custom-fabricated transparent acrylic pressure vessel (inner diameter: 8.0 cm; height: 90 cm) to simulate formation conditions. Alg-gel was injected into the packed column and subjected to an initial nitrogen pressure of 0.2 MPa. The pressure was controlled using a high-precision pressure regulator (Model YQY-12, Shanghai Zhenzhi Instrument Co., Ltd., China). After gel injection, the vessel was maintained under static conditions for a series of predefined gelation intervals (30, 60, 90, 120, 150, and 180 min). To ensure that

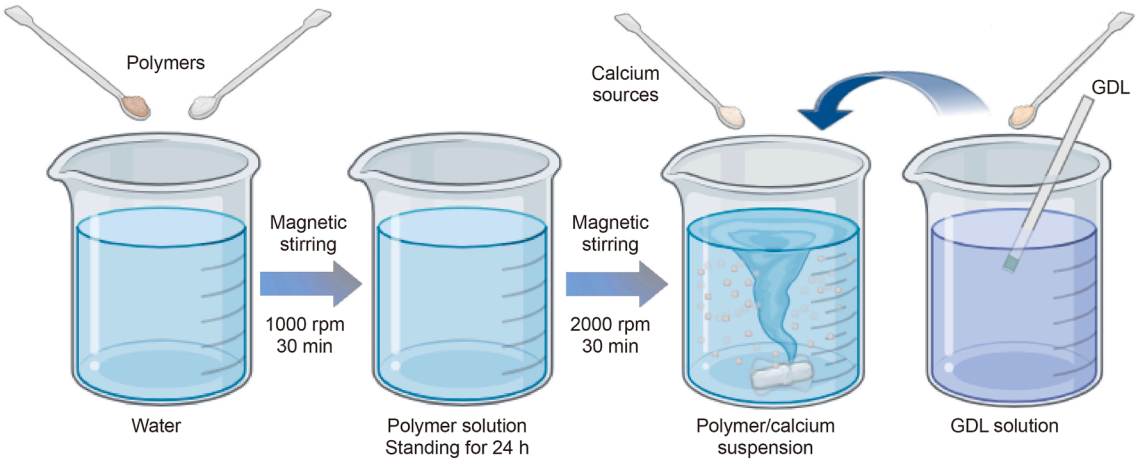

Fig. 1. Preparation procedure of the Alg-gel.

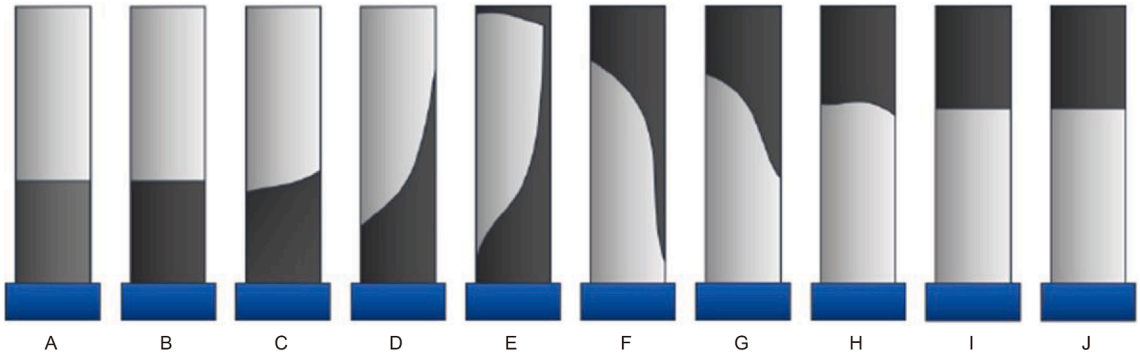

Fig. 2. Schematic illustration of the Sydansk bottle method.

the observed plugging behavior originated from hydrogel gelation rather than viscosity or solid content alone, 150 mL of a control drilling fluid, formulated to match the apparent viscosity of pre-gelled Alg-gel, was employed as a reference. Following this, 300 mL of a 3.0 wt% blue lnk solution was carefully layered onto the fluid surface to facilitate visual tracking of fluid penetration. Finally, the vessel was pressurized to 3.5 MPa using nitrogen, and the cumulative fluid loss was continuously recorded to quantify the sealing efficacy of each hydrogel formulation.

3. Results and discussion

3.1. Adhesion and rheological properties of Alg-gel

While effective fracture sealing requires hydrogels with tunable rheology and gelation kinetics, simultaneously ensuring pumpability and high mechanical strength remains a challenge (Qin et al., 2023). Here, we quantitatively investigate the effects of semi-IPN polymer composition, calcium source, and GDL concentration on the in situ gelation kinetics, rheological properties, and structural strength of Alg-gel.

3.1.1. Influence of composite polymer on adhesion and rheological properties

Multi-network hydrogels leverage dense chain entanglement and energy dissipation mechanisms to enhance stretchability and fracture-sealing performance under hydrostatic stress (Norioka et al., 2021). In this study, six gel-forming polymers were integrated with SA to improve network density and stiffness via intermolecular hydrogen bonding. To assess adhesion performance, gravel cuttings (3.5–15.0 mm) were compacted into cylindrical molds (80 mm diameter × 170 mm height), and hydrogel precursors containing 0.6 wt% SA, 0.6 wt% auxiliary polymer (agar, Cur, Cmcs, gel, or Ppcs), 3.0 wt% $CaCO_3$, and 0.03 mol/L GDL were injected into the molds and gelled in situ.

Control samples with 1.2 wt% SA alone developed macroscopic cracks (Fig. 3(a)), indicating that a mono-coordination network fails to achieve adhesion or sealing effect. Similarly, 1.2 wt% Hpg formed loose, collapsed gravel layers (Fig. 3(b)), indicating weak Ca^{2+}-carboxyl coordination insufficient for robust network assembly. Composite hydrogels containing 0.6 wt% SA with 0.6 wt% Cur, Cmcs, Ppcs or agar also yielded non-cohesive gels (Fig. 3(c)–(f)). This failure was attributed to the lack of covalent crosslinking between SA and auxiliary polymers, as well as a reduced density in Ca^{2+} chelation density, collectively hindering the formation of stable gel networks. In contrast, the SA/gel hydrogel (Fig. 3(g)) exhibited improved adhesion performance, attributed to the formation of a semi-interpenetrating network via electrostatic interactions between positively charged amino acid residues of gelatin and negatively charged carboxylate groups in alginate (Wang et al., 2021b). However, the resulting hydrogel remained soft and prone to disintegration, limiting practical applicability. Notably, the SA/Hpg hydrogel (Fig. 3(h)) formed a compact, crack-free sealing structure that effectively encapsulated the gravel layer. This enhanced mechanical integrity and adhesive performance are ascribed to the uniform interpenetrating polymer network and homogeneous Ca^{2+} crosslinking, which synergistically promote energy dissipation and network stability (Wang et al., 2021a; Zhang et al., 2024).

Furthermore, the storage modulus (G') and loss modulus (G'') of the hydrogels after 180 min of gelation were evaluated using rheological measurements. As shown in Fig. 4(a), amplitude sweep tests (strain range: 0.01%–1000%, frequency: 1.0 Hz) indicated a linear regime up to 1% strain, beyond which G' decreased and crossed G'', indicating a transition from elastic to viscous behavior due to network disruption. Accordingly, a strain of 1% was selected for the subsequent frequency sweep experiments.

As shown in Fig. 4(b), all hydrogels exhibited solid-like behavior ($G' > G''$) across the entire frequency range, confirming successful Ca^{2+} crosslinking. However, compared to pure SA, G' in SA/Ppcs, SA/agar, SA/Cmcs and SA/Cur composites decreased from 934.7 to 774.4, 487.0, 588.3, and 222.4 Pa, respectively, at 20 Hz, due to these polymers failing to form sufficiently crosslinked networks with SA. This decline in G' correlates with the weak and fragile structures observed in Fig. 3(c)–(f). Although G' of SA/gel slightly increased to 1167.0 Pa, this enhancement remained inadequate for structural plugging applications (Fig. 3(g)). Notably, the SA/Hpg composite exhibited a marked increase in G' to 2396.3 Pa, representing a 156.4% improvement, consistent with its enhanced adhesion performance shown in Fig. 3(h). The results suggest that synergistic network formation in the SA/Hpg system, facilitated by uniform polymer interpenetration and efficient Ca^{2+} chelation, substantially reinforces the hydrogel networks and improves fracture-sealing efficiency.

To identify an optimal polymer ratio, the influence of SA:Hpg ratios on rheological properties and gelation behavior was systematically examined. As illustrated in Fig. 5(a), all samples exhibited typical viscoelastic characteristics with G' consistently exceeding G'', indicating the formation of solid-like network structure during gelation. Pure SA hydrogels exhibited a G' of 934.7 Pa at 20 Hz, whereas pure Hpg hydrogels showed significantly lower G' of 196.6 Pa, reflecting insufficient structural integrity without SA. Introducing Hpg at SA:Hpg ratios of 9:1 and 7:3 increased G' to 1199.9 and 1658.0 Pa, respectively, indicating enhanced elasticity from synergistic polymer entanglements. Notably, the SA_5/Hpg_5 of a ratio of 1:1 yields the highest G' of

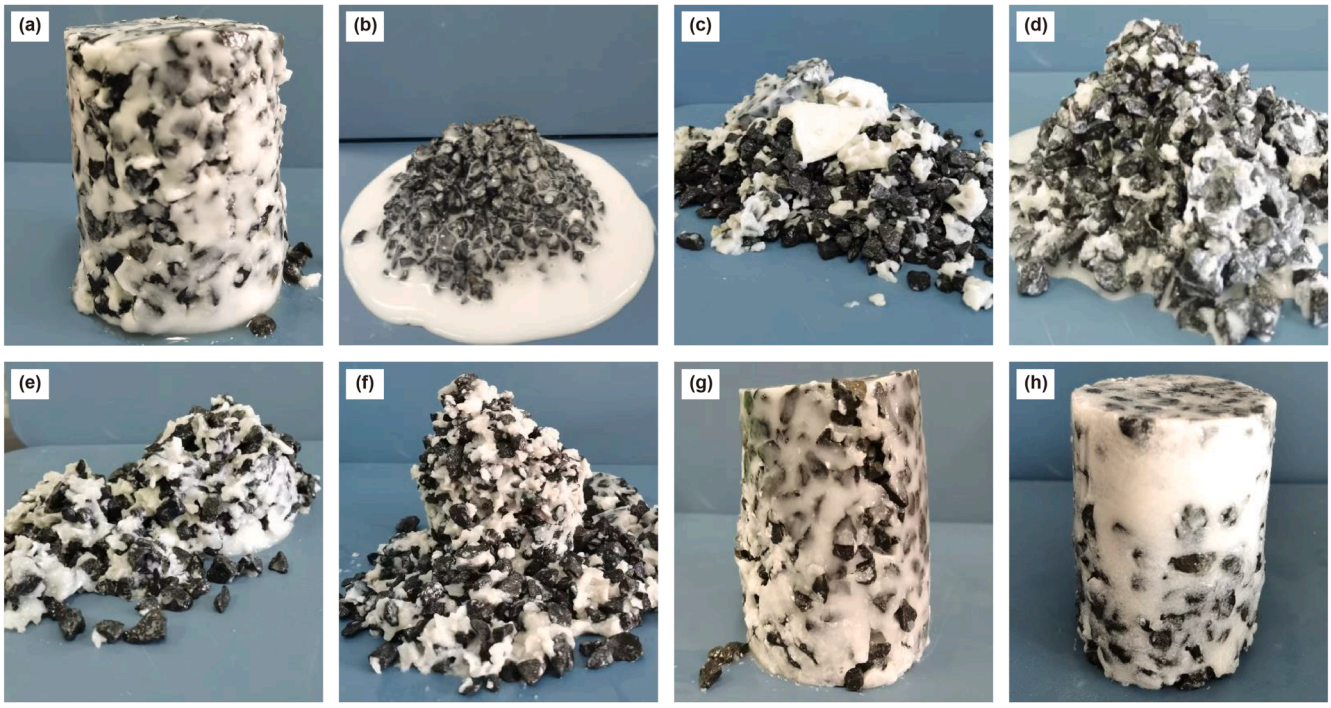

Fig. 3. Photographs showing the gravel fragments attached with various hydrogel: (**a**) 1.2 wt% SA, (**b**) 1.2 wt% Hpg, (**c**) 0.6 wt% Cur + 0.6 wt% SA, (**d**) 0.6 wt% Cmcs + 0.6 wt% SA, (**e**) 0.6 wt% Ppcs + 0.6 wt% SA, (**f**) 0.6 wt% agar + 0.6 wt% SA, (**g**) 0.6 wt% gel + 0.6 wt% SA, (**h**) 0.6 wt% Hpg + 0.6 wt% SA.

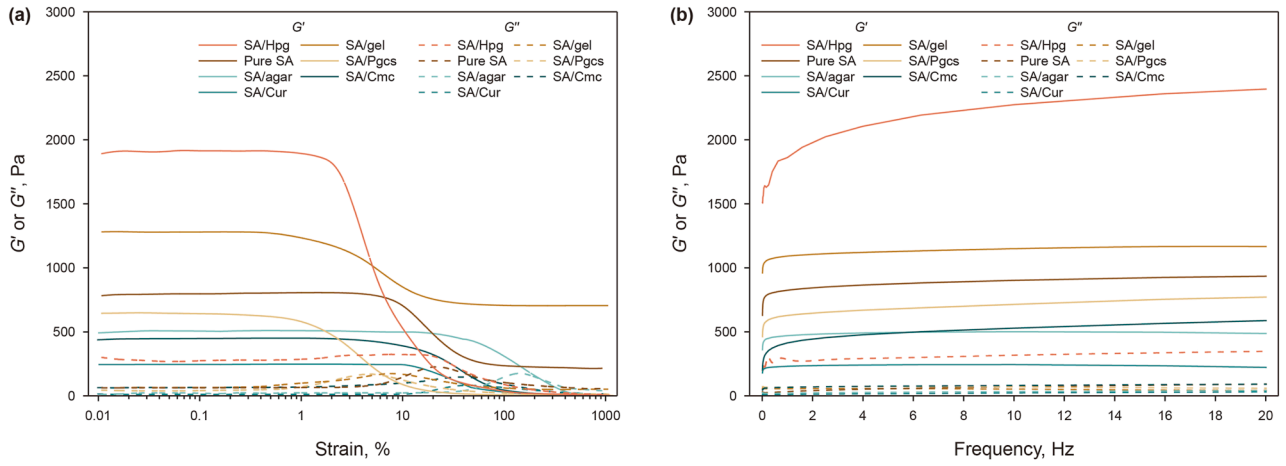

Fig. 4. Dynamic strain sweeps (**a**) and dynamic frequency sweeps (**b**) of hydrogel with different composite polymers.

2396.3 Pa, demonstrating superior energy storage and resistance to deformation. Moreover, G' remained frequency dependent, confirming sustained solid-like behavior. However, excessive Hpg content in SA_3/Hpg_7 and SA_1/Hpg_9 resulted in G' declined to 1658.0 and 222.4 Pa, respectively, due to insufficient SA content for effective Ca^{2+} crosslinking. In conclusion, the interpenetrating polymer network formed at a 1:1 of SA:Hpg ratio significantly reinforces the chelated structure, offering promising potential for enhancing pressure-bearing performance.

To further explore the influence of polymer composition on pumpability and sealing performance, the evolution of G' and G'' was tracked over different gelation intervals (Fig. 5(b)). Pure Hpg showed a slight increase in G' from 35.5 to 191.7 Pa from 30 to 180 min, reflecting a loose network due to insufficient Ca^{2+} chelation sites (Liu et al., 2024). Similarly, pure SA exhibited a modest G' increase from 396.6 to 634.7 Pa, likely due to early-stage network densification (at 30 min) that hindered subsequent Ca^{2+} diffusion and crosslinking. Reducing SA content in SA_9/Hpg_1 and SA_7/Hpg_3 formulations moderate the chelation rate, promoting more uniform network development and yielding higher final G' of 1134.7 and 1658.0 Pa, respectively. Notably, SA_5/Hpg_5 exhibited a low initial G' of 105.3 Pa at 30 min, indicative of a loosely entangled early-stage network that facilitated Ca^{2+} diffusion and subsequent chelation with SA chains. This facilitated the formation of a homogeneous and mechanically robust hydrogel, achieving a peak G' of 2396.3 Pa at 180 min. By contrast, further reducing SA content in SA_3/Hpg_7 and SA_1/Hpg_9 led to insufficient crosslinking due to the limited availability of chelating sites, resulting in lower final G' values of 1140.5 and 222.4 Pa, respectively.

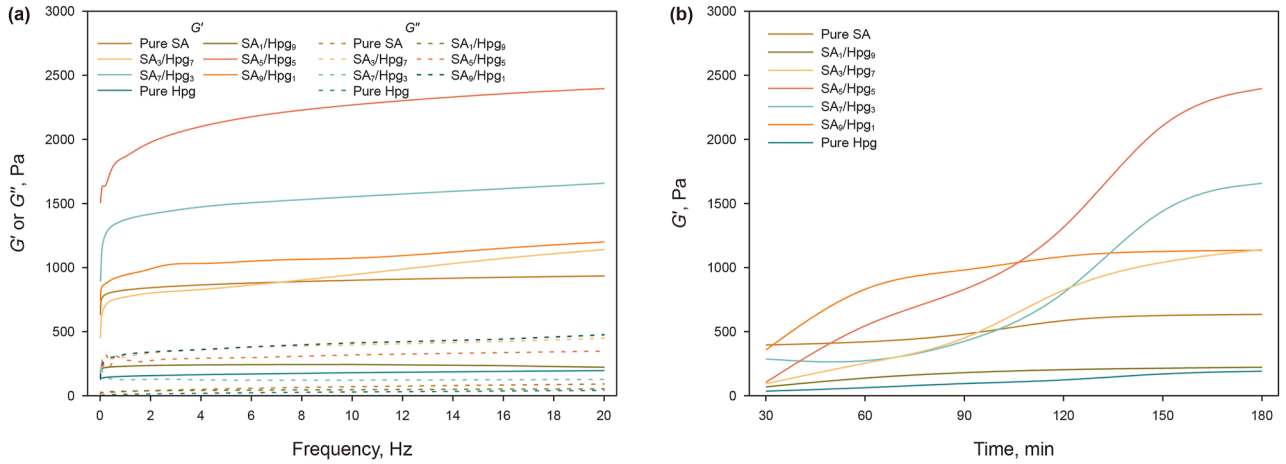

Fig. 5. (**a**) Dynamic frequency sweeps of hydrogel with different composite polymer proportions and (**b**) the variation of G' over gelation time.

These results demonstrate that adjusting the polymer ratio, particularly by reducing the relative SA content, can effectively slow the Ca^{2+} chelation kinetics, promoting sustained ion diffusion and more uniform gelation. The 1:1 SA:Hpg ratio offers a favorable trade-off by combining lower initial G' for pumpability with higher final G' for robust plugging, making it optimal for strengthening wellbore stability in practical applications. Accordingly, we adopted the 1:1 formulation for all subsequent experiments.

3.1.2. *Influence of Ca^{2+} source on adhesive performance*

To construct a homogeneous multi-network structure, different Ca^{2+} sources were employed to regulate the crosslinking process and improve network uniformity, hydrogels crosslinked with $CaCl_2$ and CL were prepared as control formulations.

As shown in Fig. 6(a1) and (b1), both $CaCl_2$ and CL triggered gels exhibited weak adhesion and displayed fragmented, porous morphologies (Fig. 6(a2) and (b2)), resulting from rapid, non-uniform Ca^{2+} chelation upon direct contact with alginate chains. Correspondingly, their LVR were narrow, with strain limits of only 0.4%, and G' values of 620.9 and 776.1 Pa, respectively (Fig. 6(d)), indicating poorly structured networks. In contrast, the GDL–$CaCO_3$ strategy yielded a hydrogel with markedly improved adhesion and a smooth, crack-free surface (Fig. 6(c1) and (c2)), reflecting the formation of a dense, cohesive microstructure. The G' reached 2396.3 Pa at 20 Hz, representing increases of 285.9% and 208.7% relative to $CaCl_2$ and CL based gels, respectively.

This enhancement is attributed to the gradual Ca^{2+} release facilitated by GDL hydrolysis, which suppresses crosslinking heterogeneity and promotes uniform network assembly.

3.1.3. *Gelling time regulation of Alg-gel*

The chelation rate of the GDL-triggered strategy is highly governed by the particle size of $CaCO_3$ microparticles (Hu et al., 2021; Lin et al., 2023). Smaller particle size with larger specific surface areas could accelerate acid-triggered Ca^{2+} release, thereby influencing gelation kinetics.

To investigate the effect of $CaCO_3$ particle size on rheological characteristics and gelation time, particle size distribution analysis was first conducted. As shown in Fig. 7(a), $CaCO_3$ particles with mesh sizes of 375, 600, 800, 1000, and 1250 corresponded to median particle diameters (D_{50}) of 38.0, 22.1, 16.8, 13.9, and 11.8 μm, according to ASTM standards. All hydrogels exhibited typical viscoelastic behavior, with G' consistently exceeding G'' across 0–20 Hz, confirming successful sol–gel transitions. The hydrogel prepared with 38.0 μm $CaCO_3$ exhibited G' of 789.51 Pa, which increased to 1593.14 and 2396.34 Pa as the D_{50} decreased to 22.1 and 16.8 μm, respectively. Nevertheless, further reductions in D_{50} to 13.9 and 11.8 μm resulted in decreased G' values of 2076.60 and 1265.05 Pa, respectively, suggesting that excessively rapid gelation impeded subsequent Ca^{2+} diffusion and hindered the development of a dense three-dimensional network (Fig. 7(b)). The time-dependent evolution of G' further supports these observations. Hydrogels incorporating 38.0 and 22.1 μm $CaCO_3$ showed low initial G' values (100.2 and 156.6 Pa at 30 min), gradually increasing to 789.5 and 1593.1 Pa at 180 min, respectively. Notably, the 16.8 μm group exhibited a moderate initial G' of 245.3 Pa but reached the highest final G' of 2396.3 Pa, indicating an optimal balance between early-stage crosslinking and sustained Ca^{2+} migration. In contrast, hydrogels prepared with 13.9 and 11.8 μm $CaCO_3$ showed relatively high initial G' values (601.90 and 706.34 Pa at 30 min) but exhibited lower final G' values of 2076.0 and 1528.4 Pa at 180 min (Fig. 7(c)). This trend suggests that overly rapid crosslinking may cause local Ca^{2+} entrapment, impeding ion diffusion and compromising network uniformity.

In summary, $CaCO_3$ particle size critically regulates gelation kinetics and final mechanical strength. While finer particles enhance Ca^{2+} release, excessive reactivity can induce premature gelation and structural heterogeneity. A D_{50} of 16.8 μm offered the best trade-off between pumpability and final G', and was thus adopted in subsequent formulations.

To further investigate the influence of $CaCO_3$ concentration on rheological characteristics at different gelation stages (Fig. 8), frequency sweep measurements were conducted across a range of $CaCO_3$ contents (1.0–5.0 wt%).

At 30 min, G' values were 207.6, 222.4, and 245.3 Pa in $CaCO_3$ concentrations of 1.0, 2.0, and 3.0 wt%. Further increasing the $CaCO_3$ concentration to 4.0 and 5.0 wt% slightly elevated initial G' to 293.5 and 373.0 Pa, suggesting that excessive $CaCO_3$ did not substantially enhance the hydrogel network density at the early stage. By 90 min, the G' of the 1.0, 2.0, and 3.0 wt% formulations increased modestly to 340.6, 572.0, and 793.7 Pa, while 4.0 and 5.0 wt% samples exhibited sharp increases to 1518.8 and 2048.7 Pa, respectively, indicating accelerated gelation. However, this rapid early crosslinking may impede subsequent Ca^{2+} diffusion. At 180 min, the G' values in 1.0, 2.0, and 3.0 wt% groups continued to increase steadily, reaching 856.0, 1538.2, and 2396.3 Pa, respectively. In contrast, the 4.0 wt% group plateaued at 2451.5 Pa, while 5.0 wt% declined to 2114.8 Pa, likely due to the premature formation of a dense and compact gel layer, which hinders further

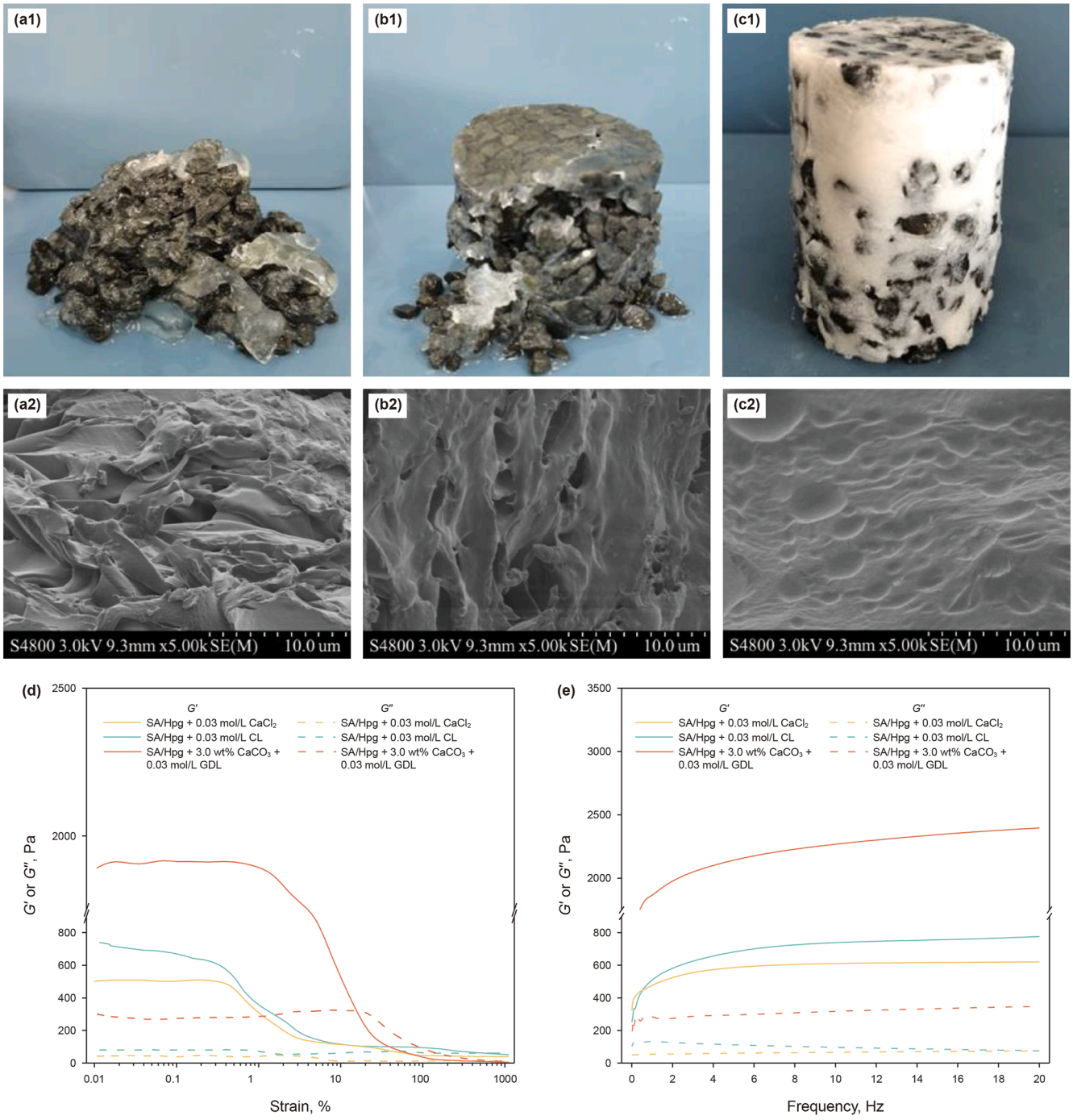

Fig. 6. Photographs of simulated gravel formations attached with hydrogels prepared using $CaCl_2$ (**a1**), CL (**b1**), and the GDL-$CaCO_3$ strategy (**c1**), along with corresponding SEM images (**a2**, **b2**, and **c2**), and dynamic strain sweep (**d**) and dynamic frequency sweep (**e**) results.

Ca^{2+} migration and chelation, ultimately limiting full network development.

Taken together, our results show that both $CaCO_3$ particle size and concentration exert a decisive influence on the gelation behavior of the GDL-triggered system. Particle size governs the rate and uniformity of Ca^{2+} release: excessively fine particles (< 14 μm) accelerate hydrolysis but promote premature local crosslinking and structural heterogeneity, whereas overly coarse particles (> 22 μm) delay gelation and limit network strength. Likewise, $CaCO_3$ concentration sets the balance between early-stage gelation and long-term uniformity: contents ≥ 4 wt% steepen the initial G' growth yet hinder sustained Ca^{2+} migration, compromising network maturation. On this basis, we selected $D_{50} = 16.8$ μm at 3.0 wt% $CaCO_3$ as the optimal trade-off between pumpability, gelation kinetics, and final mechanical strength, and adopted these parameters for subsequent experiments.

Previous studies (Ben Djemaa et al., 2024) have highlighted the critical role of GDL in regulating Ca^{2+} release through GDL-$CaCO_3$ strategy. To further elucidate this effect, hydrogels were prepared using GDL concentrations between 0.01 and 0.05 mol/L (Fig. 9(a)).

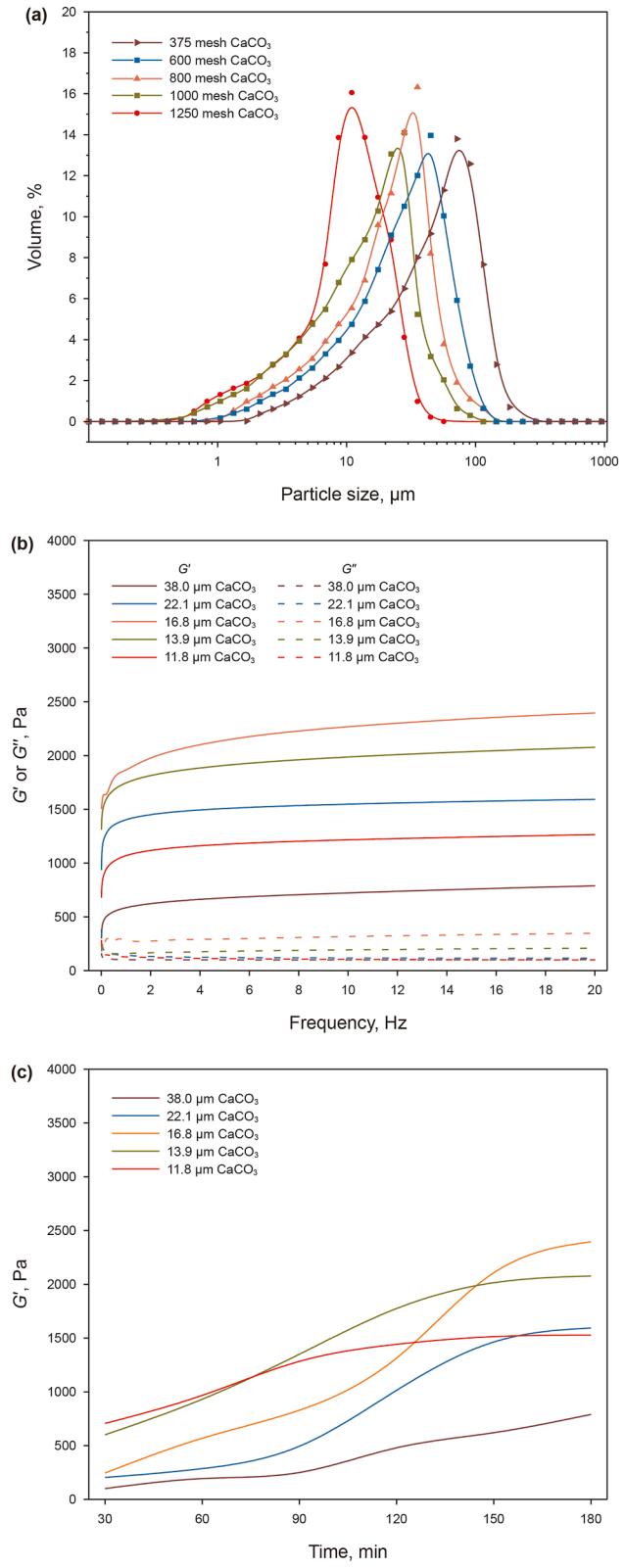

Fig. 7. Particle size distribution of $CaCO_3$ (**a**) and the corresponding dynamic frequency sweeps (**b**) as well as the dynamic time sweeps (**c**) of hydrogel.

At 30 min, the initial G' values increased progressively from 173.7 to 607.9 Pa as the GDL concentration increased, reflecting an acceleration of early crosslinking. By 90 min, G' continued to rise steadily in the 0.01–0.03 mol/L groups (376.4–793.7 Pa), whereas sharp increases were observed for the 0.04 and 0.05 mol/L samples, reaching 1785.4 and 1856.3 Pa, respectively. At 180 min, G' reached 756.5, 1756.1, and 2396.3 Pa for 0.01–0.03 mol/L, confirming continuous network development. In contrast, the 0.04 and 0.05 mol/L groups plateaued earlier (around 120 min), yielding final G' values of 2412.4 and 2147.7 Pa. This suggests that excessive GDL caused overly rapid Ca^{2+} release, producing a dense outer layer that impeded further ion diffusion and network maturation.

Taken together, gelation kinetics and final rheological characteristics were strongly governed by Ca^{2+} release rate and could be effectively modulated by adjusting polymer composition, Ca^{2+} source, $CaCO_3$ particle size and concentration, as well as the GDL content. Based on the above findings, the optimized formulation that balances pumpability and plugging performance was identified as follows: 0.6 wt% SA, 0.6 wt% Hpg, 3.0 wt% $CaCO_3$, and 0.03 mol/L GDL.

3.2. Synergistic gelation mechanism analysis

3.2.1. FTIR spectroscopy

To further verify Ca^{2+} chelation with SA/Hpg chains and the formation of a multi network structure in Alg-gel, FT-IR spectra of Alg-gel, SA, Hpg and their binary blend (SA/Hpg) were analyzed (Fig. 10).

For Hpg, the broad absorption band at 3421 cm^{-1} corresponds to O–H stretching vibrations, while the peak at 2926 cm^{-1} arises from asymmetric C–H stretching (Lu et al., 2019). The band at 1585 cm^{-1} is assigned to H–O–H bending, and the peak at 1413 cm^{-1} corresponds to in-plane C–H bending vibrations (Yin et al., 2018). In SA, the O–H stretching band appears at 3408 cm^{-1}, and the peak at 2950 cm^{-1} is attributed to C–H stretching (Wang et al., 2022). Additionally, the characteristic $–COO^-$ asymmetric and symmetric stretching bands are observed at 1601 and 1395 cm^{-1}, respectively, originating from the saccharide backbone. In the SA/Hpg blend, the O–H stretching band of SA shifts from 3408 cm^{-1} to a higher wavenumber (3455 cm^{-1}) with reduced intensity, indicating hydrogen bond formation between SA and Hpg. Moreover, the $–COO^-$ stretching bands shift from 1601 and 1395 cm^{-1} to 1612 and 1423 cm^{-1}, respectively, which constitutes the formation of a hydrogen-bonded semi-interpenetrating network, constituting the first structural framework in Alg-gel. Compared with the SA/Hpg blend, Alg-gel exhibits a further reduction in O–H stretching intensity, attributed to the chelation between hydroxyl/carboxyl groups and Ca^{2+} (Lin et al., 2023). The substitution of Na^+ with Ca^{2+} modifies the ionic environment, shifting the $–COO^-$ bands to lower wavenumbers at 1581 and 1388 cm^{-1}. Additionally, peaks at 709 and 871 cm^{-1}, characteristic of CO_3^{2-}, indicate the partial presence of unreacted $CaCO_3$ particles.

Collectively, these spectral features confirm the successful construction of a hierarchical multi-network structure, comprising a hydrogen-bonded semi-interpenetrating polymer network and a Ca^{2+}-coordinated ionic crosslinking network. This multilevel architecture highlights the effectiveness of the GDL-triggered strategy in enhancing structural cohesion and mechanical integrity, as further corroborated by subsequent SEM observations.

3.2.2. Morphology analysis of Alg-gel

Fig. 11 illustrated the microstructural evolution of Alg-gel at different gelation intervals, together with the corresponding sol–gel conversion stages in the inverted bottle test, offering a convincing visual approach to evaluate adhesion performance over time (Bai et al., 2022b; Chen et al., 2024; Xie et al., 2021).

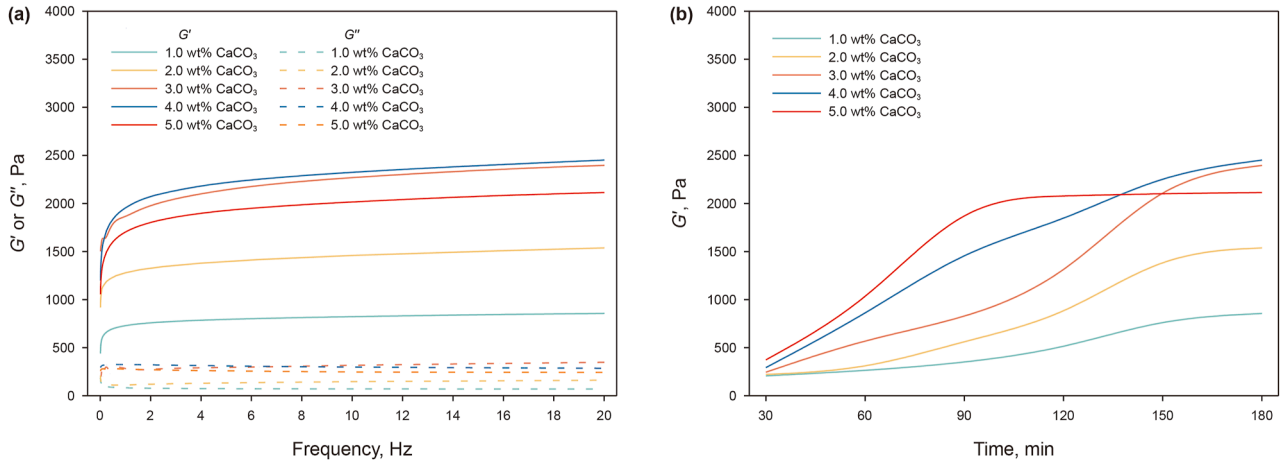

Fig. 8. (**a**) Dynamic frequency sweeps of Alg-gel with different $CaCO_3$ concentrations; (**b**) the variation of G' over gelation time.

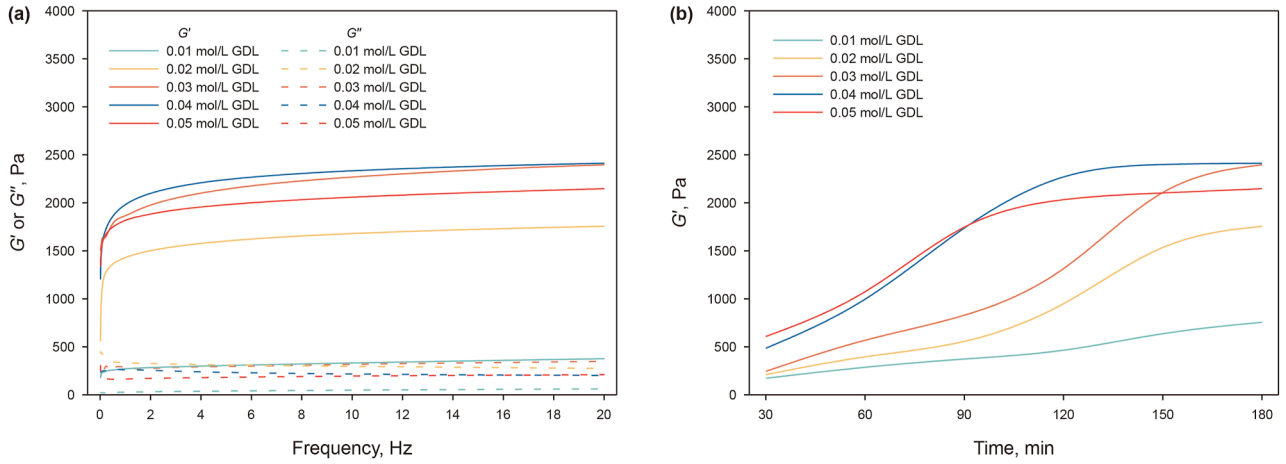

Fig. 9. (**a**) Dynamic frequency sweeps of Alg-gel with different GDL concentrations; (**b**) G' over gelation time.

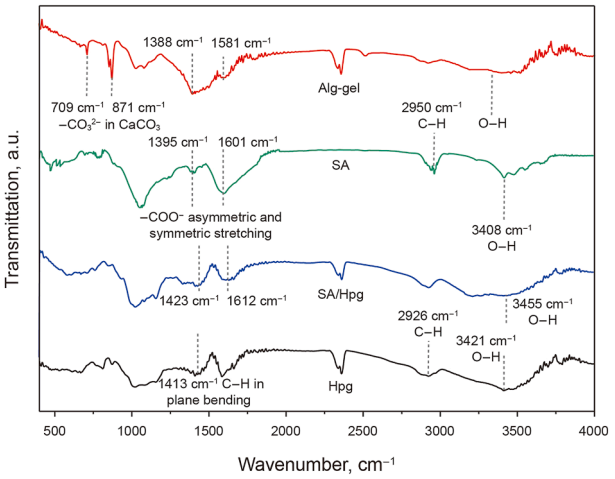

Fig. 10. FTIR spectra of Alg-gel, SA, SA/Hpg, and Hpg.

At 30 min, a loose filamentous matrix embedded with $CaCO_3$ particles formed a porous network, exhibiting minimal wall adhesion and insufficient cohesion. As gelation progressed to 60 and 90 min, the network became denser, gradually filling pore spaces and forming multilayered dendritic structures, which coincided with enhanced adhesion. At 120–150 min, smoother surfaces with $CaCO_3$ protuberances and reduced filamentous features appeared, indicating polymer compaction. This stage coincided with stronger gel adhesion, evidenced by visible deformation and greater wall adherence in the inverted bottle test. After 180 min, Alg-gel formed a continuous, compact hydrogel barrier with high deformation resistance, reflecting the completion of network crosslinking and structural integration.

This progression confirms that Alg-gel transitions from a loose polymer–$CaCO_3$ composite into a densely crosslinked network via GDL-triggered Ca^{2+} release. $CaCO_3$ particles function both as pH-responsive calcium reservoirs that sustain "egg-box" ionic crosslinking, and as rigid physical bridges embedded within the polymer matrix. These multiple roles collectively reinforce structural integrity and enhance plugging efficacy during the entire gelation process.

3.2.3. *pH variation and Ca^{2+} concentration as a function of time*

As discussed above, the gelation behavior of the GDL-triggered strategy is predominantly governed by acidification kinetics, which regulate both pH reduction and the associated release of Ca^{2+} from $CaCO_3$. To elucidate this mechanism, the temporal variations in pH and Ca^{2+} concentration of the optimized formulation were monitored using a pH meter and EDTA titration.

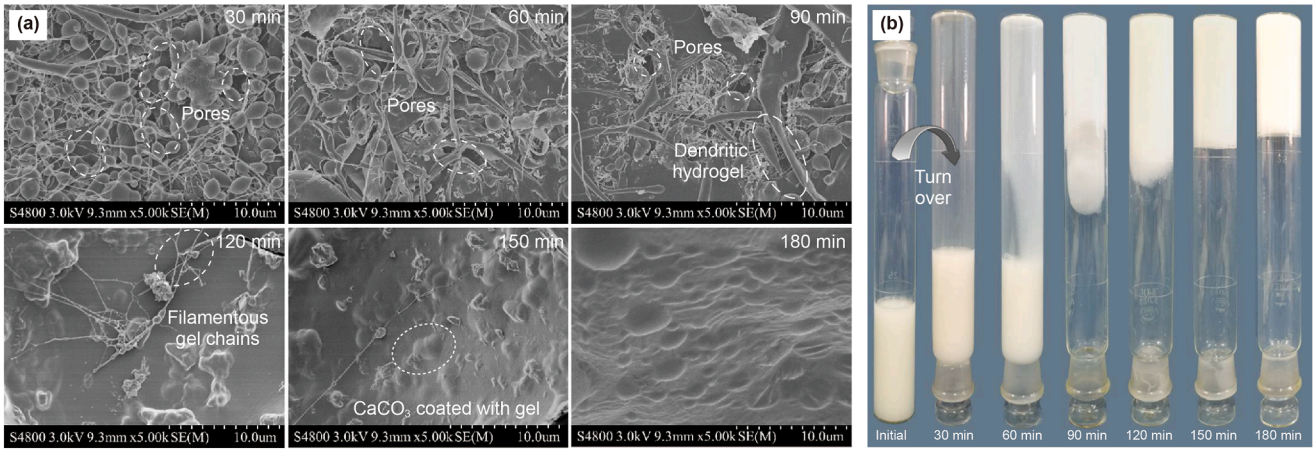

Fig. 11. SEM images of Alg-gel at different gel time (**a**) and their inverted photographs tested by sydansk bottle method (**b**).

As illustrated in Fig. 12, the initial pH of water was 7.2. Upon the addition of 0.01, 0.02, and 0.03 mol/L GDL, the pH dropped to 3.9, 3.6, and 3.3, respectively, after 90 min, owing to partial hydrolysis of GDL. Correspondingly, Ca^{2+} concentrations increased to 3.2, 3.6, and 4.0 mmol/L. At higher GDL concentrations (0.04 and 0.05 mol/L), acidification occurred more rapidly, lowering the pH to 2.8 and 2.6 and increasing Ca^{2+} concentrations to 4.7 and 5.0 mmol/L, respectively. At 180 min, the hydrolysis rate of GDL slowed, with pH values stabilizing at 3.4, 3.1, and 2.8 for the 0.01, 0.02, and 0.03 mol/L groups, and Ca^{2+} concentrations rising modestly to 3.9, 4.4, and 4.9 mmol/L, respectively. In the 0.04 and 0.05 mol/L groups, further acidification decreased pH values to 2.3 and 2.2, with Ca^{2+} concentrations reaching 6.5 and 5.9 mmol/L, respectively.

These results confirm that the GDL-triggered acidification process enables controlled Ca^{2+} release from $CaCO_3$ through the gradual hydrolysis of GDL. This demonstrates that the approach provides a viable and controllable means of modulating gelation kinetics and improving the structural integrity of the hydrogel.

3.2.4. Multi network gelation mechanism

Fig. 13 illustrates the gelation mechanism of Alg-gel, which involves the cooperative action of a semi-interpenetrating network, Ca^{2+}-mediated ionic crosslinking, and embedded $CaCO_3$ particle reinforcement. At the molecular level, FTIR spectra confirmed that intra- and intermolecular hydrogen bonding between SA and Hpg chains formed a primary semi-interpenetrating polymer network, as evidenced by the shift of O–H and –COO– stretching bands. These hydrogen-bonded interactions offered abundant coordination sites for Ca^{2+} crosslinking and provided the initial structural framework of the hydrogel. Subsequently, the gradual hydrolysis of GDL triggered controlled acidification, which was directly reflected in the measured decrease of pH and the concomitant increase in Ca^{2+} concentration over time (Fig. 12). This regulated release of Ca^{2+} from dispersed $CaCO_3$ particles facilitated their chelation with the polymeric backbone, thereby inducing the formation of the secondary “egg-box” architecture. The kinetics of Ca^{2+} liberation ensured a progressive and controllable gelation process, allowing the network to densify gradually. SEM observations further corroborated this sequential mechanism by showing that the initial loose polymer–$CaCO_3$ composite progressively transformed into a compact and continuous hydrogel matrix. In this structure, $CaCO_3$ particles not only acted as calcium reservoirs sustaining ionic crosslinking but also served as rigid bridges embedded within the polymer framework, thus enhancing structural integrity and plugging efficacy.

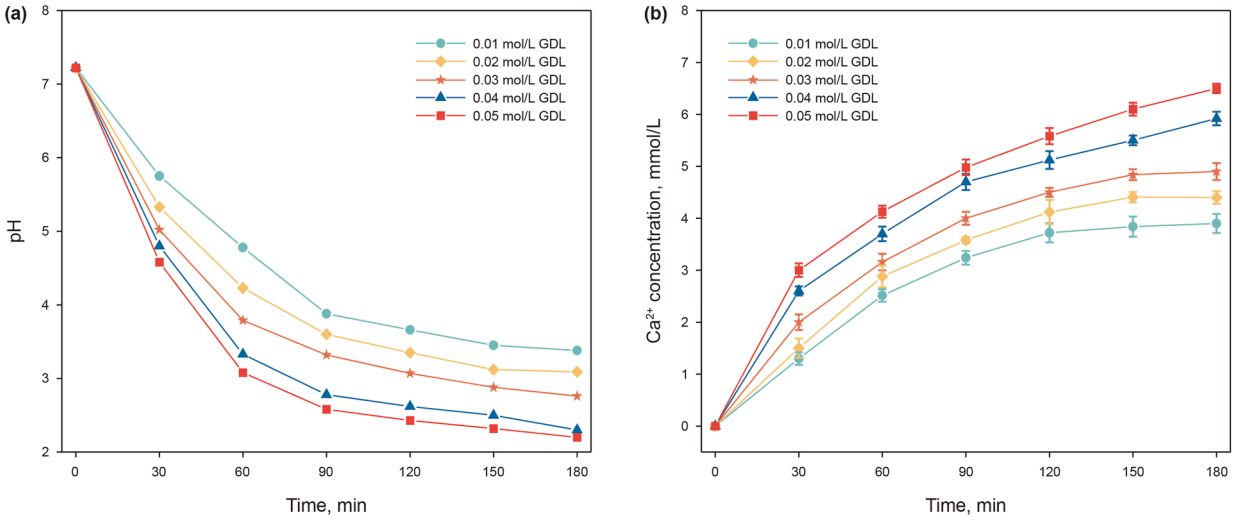

Fig. 12. Variations in pH (**a**) and Ca^{2+}concentration (**b**) at different gelation time intervals.

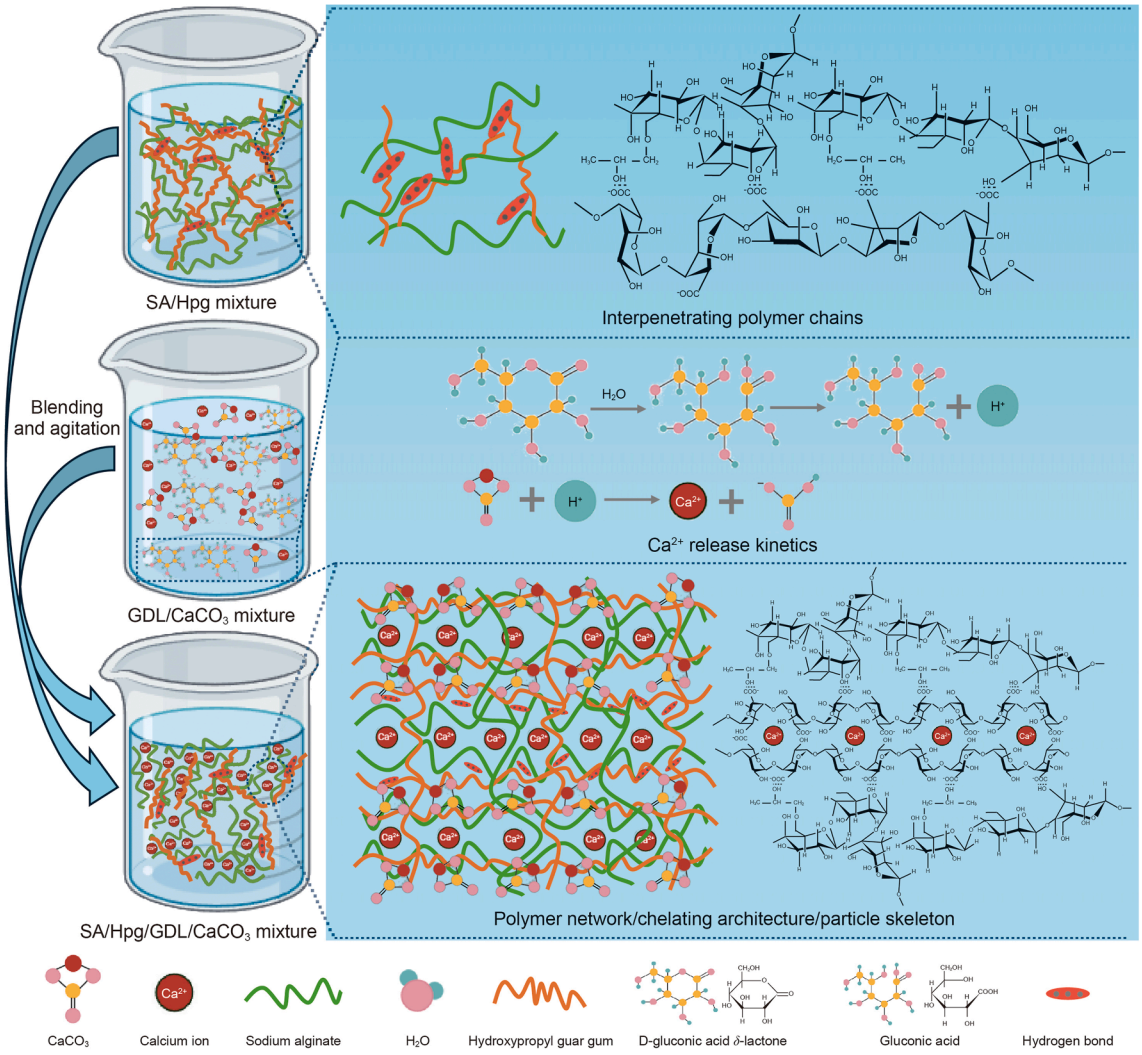

Fig. 13. Synergistic gelation mechanism diagram of Alg-gel.

Taken together, these results demonstrate that Alg-gel undergoes a stepwise gelation process in which hydrogen-bond-driven semi-interpenetrating networks are first established, followed by GDL-mediated Ca^{2+} release that induces ionic crosslinking, and finally reinforced by the physical embedding of residual $CaCO_3$ particles. This hierarchical multi-network architecture accounts for the enhanced cohesion, mechanical integrity, and plugging efficacy of Alg-gel, enabling it to function as a robust waterproof barrier that strengthens wellbore stability.

3.3. Plugging performance of Alg-gel

Alg-gel demonstrates superior adhesion and sealing performance by forming a compact barrier layer via multi-network crosslinking. To evaluate its practical plugging efficacy under heterogeneous conditions, shale, gravel, and basalt cuttings were employed as formation analogs to simulate varying porosities. Fluid loss volumes were recorded at different gelation intervals using a high-pressure plugging apparatus maintained at a constant pressure of 3.5 MPa. For direct visualization of the plugging behavior, a transparent acrylic column was sequentially packed with cuttings and Alg-gel precursor, followed by the top-down injection of drilling fluid and dye solution.

As shown in Fig. 14(a) and (b), after 30 min of gelation in the simulated shale formation (porosity: 35.7%), almost all drilling fluid and dye solution leaked under pressure, resulting in a 60 min fluid loss volume of 508.0 mL, with minimal Alg-gel retention within the seepage channels. When the gelation time was extended to 60 and 90 min, fluid loss volumes decreased slightly to 478.1 and 412.0 mL, respectively, indicating partial pore sealing due to limited hydrogel infiltration. After 180 min of pressurization, final loss volumes decreased slightly from 515.0 mL (30 min gelation) to 494.0 and 443.0 mL, corresponding to reductions of 4.1% and 14.0%. In contrast, at gelation times of 120 and 150 min, a compact and cohesive Alg-gel layer visibly formed above the shale cuttings. This significantly reduced 60 min fluid losses to 186.9 and 85.0 mL, while final loss volumes dropped to 302.2 and 182.6 mL, representing reductions of 41.3% and 64.5%, respectively. Notably, after 180 min of gelation, a continuous, shield-like hydrogel barrier was formed, lowering fluid losses to 39.4 mL (92.2%) and 55.1 mL (89.3%) at 60 and 180 min of pressurization, respectively. These results clearly indicate that prolonged gelation time markedly enhances the plugging performance of Alg-gel by promoting sustained Ca^{2+} release and progressive network densification. The resulting robust hydrogel barrier effectively seals pores and significantly improves wellbore stability under high-porosity and fractured conditions.

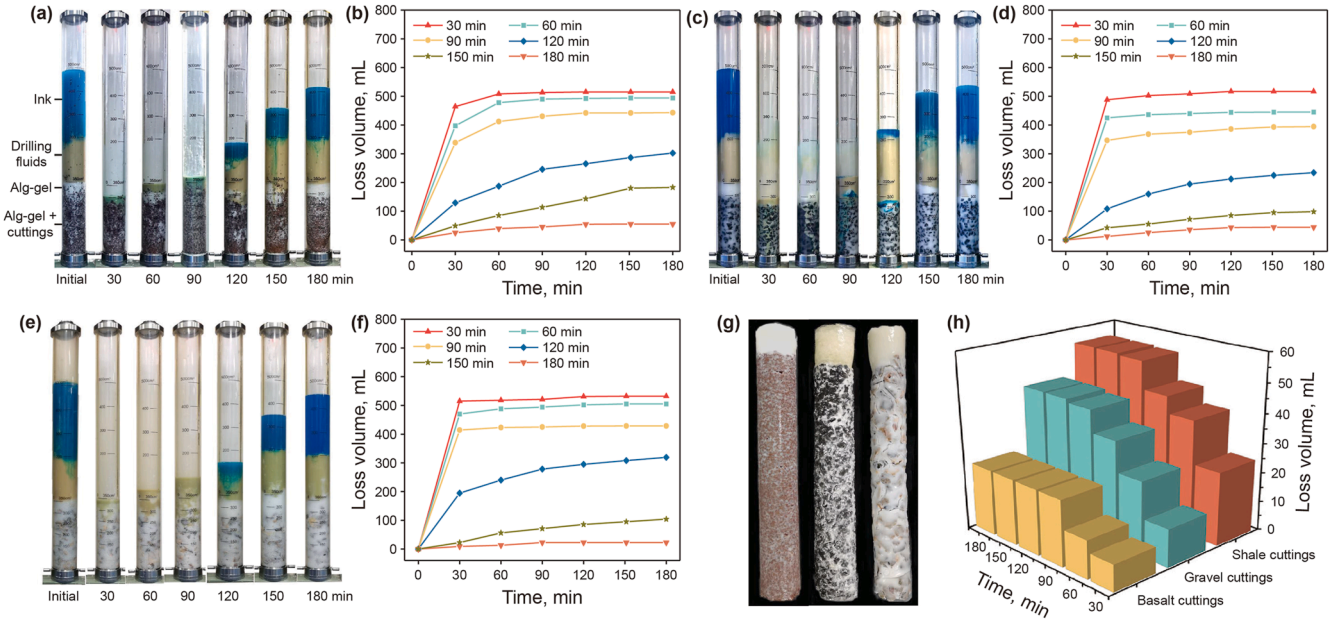

Fig. 14. Images of plugging test and corresponding loss volume curves in shale (**a**, **b**), gravel (**c**, **d**), basalt (**e**, **f**) simulated formation, and comparative loss volume profile across formations (**g**) along with photographs of formation consoli (**h**) dated by Alg-gel.

In the simulated gravel formation (porosity: 46.3%), Alg-gel exhibited limited plugging capability at 30 min of gelation, resembling the behavior observed in the shale analog. Upon pressurization, nearly all drilling fluid, dye, and hydrogel precursors leaked through the tube, resulting in a high loss volume of 517.0 mL (Fig. 14(c) and (d)). At gelation times of 60 and 90 min, small amounts of Alg-gel remained within seepage channels, but failed to establish effective barriers, with loss volumes decreasing only slightly to 445.2 and 394.4 mL, representing reductions of 13.9% and 23.7%, respectively. At 120 and 150 min, a continuous Alg-gel layer progressively formed within the pore structure, substantially reducing fluid loss to 234.0 mL (54.7%) and 98.2 mL (81.0%), respectively. At 180 min, a dense, shield-like hydrogel layer was established atop the gravel cuttings, effectively sealing pores and fractures, further reducing the loss volume to 44.0 mL with 91.5% reduction.

A similar trend was observed in the simulated basalt formation (porosity: 57.1%), where plugging performance improved steadily with gelation time (Fig. 14(e) and (f)). Loss volumes declined from 532.1 mL at 30 min to 505.2, 428.4, and 319.2 mL at 60, 90, and 120 min, corresponding to reductions of 5.1%, 19.5%, and 40.0%, respectively. At 150 and 180 min, the development of a compact, continuous Alg-gel network led to substantial sealing, with fluid losses reduced to 104.0 mL (80.5%) and 22.4 mL (95.8%). These findings demonstrate that Alg-gel can effectively form integrated physical and chemical barriers within high-porosity media, significantly limiting fluid intrusion and enhancing wellbore stability across a range of heterogeneous formation types.

Conventional LCMs demonstrate limited plugging efficacy in formations with large pores or fractures, primarily due to inadequate structural integrity (Sun et al., 2023b; Yang et al., 2019). In contrast, the consolidated images (Fig. 14(g)) reveal robust cohesive adhesion of Alg-gel across formations with varying porosities. To quantitatively assess pore-size adaptability, fluid loss volumes were compared after 180 min of gelation (Fig. 14(h)). In the shale analog (porosity: 35.7%), fluid loss increased rapidly from 25.0 to 55.1 mL under pressurization from 30 to 180 min. By comparison, the gravel formation (46.3% porosity) exhibited reduced loss volumes, increasing from 13.0 to 44.0 mL over the same period—representing a 20.2% reduction relative to the shale case. Notably, the basalt analog (57.1% porosity) exhibited the lowest fluid loss, increasing only from 9.0 to 22.4 mL, representing a 59.3% decrease compared to shale.

These results demonstrate the superior sealing capability of Alg-gel. In contrast to conventional LCMs, its plugging performance improves with increasing formation porosity. This counterintuitive behavior is attributed to the more efficient diffusion of Ca^{2+} ions within larger pore channels, which promotes enhanced ionic cross-linking and the formation of a denser, more cohesive hydrogel network. Consequently, fluid loss is markedly reduced, and wellbore stability is substantially reinforced.

3.4. Mechanical properties

The structural integrity of hydrogels under tensile and compressive loads fundamentally governs their pressure-bearing capacity in wellbore stabilization (Yang et al., 2022). Fig. 15 illustrates the evolution of Alg-gel's mechanical behavior using representative stress–strain curves, toughness, and modulus across critical gelation stage (120–180 min). Data collected below 120 min were below the detection threshold of our instrumentation, indicating insufficient network consolidation for reliable quantification.

At 120 min, the hydrogel exhibited a tensile strength of 1.60 kPa with 40.3% elongation at break, yielding a toughness of 0.41 kJ/m^3 and a modulus of 0.53 kPa. Extending gelation to 150 min elevated tensile strength 2.3-fold to 3.71 kPa while increasing elongation to 48.27%, driving toughness to 1.06 kJ/m^3 and modulus to 0.95 kPa. At 180 min, strength surged to 5.89 kPa with 57.89% elongation, producing 2.34 kJ/m^3 toughness and 2.20 kPa modulus. Compression tests confirmed consistent reinforcement, showing that compressive strength increased from 0.18 kPa (120 min) to 3.12 kPa (180 min), while elongation rose from 29.78% to 51.09%. This translated to compressive toughness enhancement from 0.11 to 0.97 kJ/m^3 and modulus from 0.30 to 1.63 kPa.

These results suggest that extended gelation time promotes progressive network densification through continuous

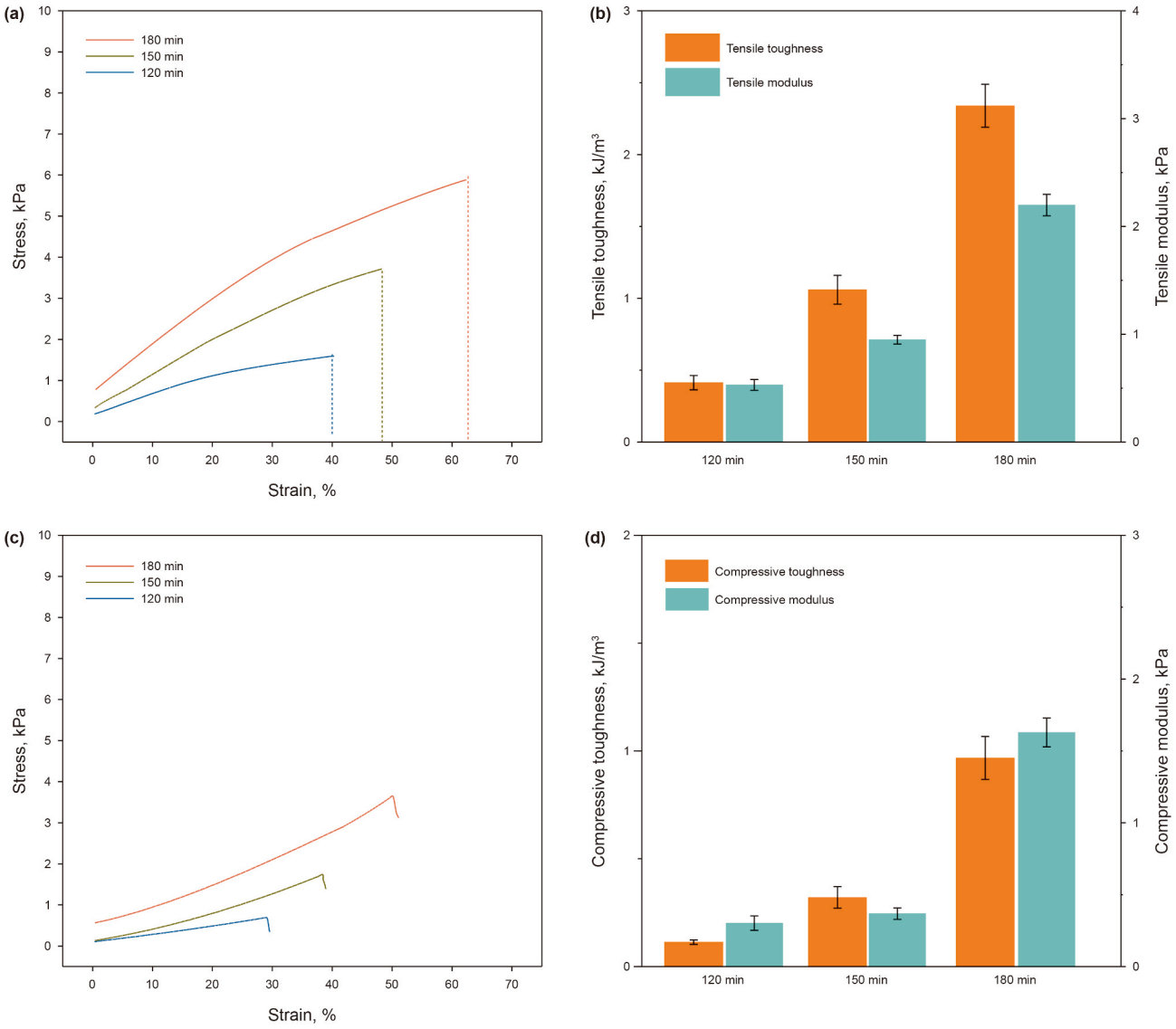

Fig. 15. Evolution of mechanical behavior of Alg-gel at different gelation times. Tensile stress–strain curves (**a**) and the corresponding tensile toughness and modulus values (**b**); compressive stress–strain curves (**c**) and the corresponding compressive toughness and modulus values (**d**).

crosslinking, thereby enhancing energy dissipation capacity and mechanical robustness. This structural evolution aligns with the compact gel architectures observed in the SEM analysis.

4. Conclusions

In this study, we developed a multi-network in situ crosslinked hydrogel by integrating sodium alginate with Hpg, GDL, and rigid $CaCO_3$ particles through an acid-triggered self-assembly strategy. This system synergistically integrates a semi-interpenetrating polymer network, Ca^{2+}-mediated ionic coordination, and particle-reinforced scaffolding, therefore constructing a structurally robust hydrogel barrier. The gelation kinetics could be precisely tuned by adjusting $CaCO_3$ particle size, concentration, and GDL dosage. Upon gradual hydrolysis, GDL lowered the pH and triggered sustained Ca^{2+} release, which promoted the formation of localized "egg-box" coordination zones. Meanwhile, the unreacted $CaCO_3$ acted as embedded rigid fillers, reinforcing the hydrogel matrix and enhancing cohesion.

The hydrogel exhibited excellent water-blocking performance, achieving an 89.3% reduction in fluid loss after 180 min of gelation. Both tensile and compressive strengths showed time-dependent enhancement, consistent with the evolution of compact and cohesive network architecture. Compared with shale (35.7% porosity), fluid loss volumes decreased from 55.1 to 44.0 mL in gravel (46.3%) and further to 22.4 mL in basalt (57.1%) after 180 min of gelation. This demonstrates that the combined effects of larger pore volumes and gradual Ca^{2+} release significantly enhance ion diffusion and promoted progressive network densification, thereby improving sealing efficacy under increasing formation porosity.

This GDL-triggered strategy, which integrates polymer entanglements, dynamic coordination, and rigid embedded skeletons, offers a promising approach for constructing high-performance hydrogels. Featuring strong adhesive interactions, tunable gelation, and porosity-adaptive sealing behavior, it represents a promising solution for mitigating wellbore instability in heterogeneous reservoirs.

CRediT authorship contribution statement

Zhao-Jie Wei: Writing – original draft, Visualization, Data curation, Conceptualization. **Ying-Long Duan:** Supervision, Methodology, Investigation. **Mao-Sen Wang:** Software, Formal

analysis. **Ying-Hui An:** Formal analysis, Data curation. **Wen-Jing Qin:** Investigation. **Ming-Yi Guo:** Investigation, Formal analysis.

Data availability

Data will be made available on request.

Declaration of competing interest

The authors declare that they have no known competing financial interests or personal relationships that could have appeared to influence the work reported in this paper.

Acknowledgments

The authors acknowledge financial support from the National Natural Science Foundation of China (No. 42072338) and the National Key Research and Development Project of China (No. 2024YFC3212100). The authors gratefully acknowledge Professor Kai-Xuan Qiu and Dr. Ying Meng from the Great Bay University for helpful suggestions and discussion on this paper.

References

Bai, B., Zhou, J., Yin, M., 2015. A comprehensive review of polyacrylamide polymer gels for conformance control. Petrol. Explor. Dev. 42 (4), 525–532. https://doi.org/10.1016/S1876-3804(15)30045-8.

Bai, Y., Zhang, Q., Sun, J., et al., 2021. Self-healing hydrogels and their action mechanism in oil–gas drilling and development engineering: A systematic review and prospect. J. Nat. Gas Sci. Eng. 96, 104250. https://doi.org/10.1016/j.jngse.2021.104250.

Bai, Y., Dai, L., Sun, J., et al., 2022a. Plugging performance and mechanism of an oil-absorbing gel for lost circulation control while drilling in fractured formations. Pet. Sci. 19 (6), 2941–2958. https://doi.org/10.1016/j.petsci.2022.08.004.

Bai, Y., Liu, C., Sun, J., et al., 2022b. High temperature resistant polymer gel as lost circulation material for fractured formation during drilling. Colloids Surf. A Physicochem. Eng. Asp. 637, 128244. https://doi.org/10.1016/j.colsurfa.2021.128244.

Bai, Y., Zhang, Q., Sun, J., et al., 2022c. Double network self-healing hydrogel based on hydrophobic association and ionic bond for formation plugging. Pet. Sci. 19 (5), 2150–2164. https://doi.org/10.1016/j.petsci.2022.07.006.

Bai, Y., Zhu, Y., Sun, J., et al., 2023. High stability polymer gel for lost circulation control when drilling in fractured oil and gas formations. Geoenergy Sci. Eng. 225, 211722. https://doi.org/10.1016/j.geoen.2023.211722.

Bakhshizadeh, A., Khayat, N., Horpibulsuk, S., 2022. Surface stabilization of clay using sodium alginate. Case Stud. Constr. Mater. 16, e01006. https://doi.org/10.1016/j.cscm.2022.e01006.

Ben Djemaa, I., Boulmedais, F., Auguste, S., et al., 2024. Glucono-delta-lactone-induced alginate gelation: New insights into the effect of the cross-linker carrier type on the hydrogel mechanics. Langmuir 40 (20), 10492–10501. https://doi.org/10.1021/acs.langmuir.3c03959.

Chen, J., Qiu, H., Djouonkep, L.D.W., et al., 2024. Preparation, evaluation and field application of thermally induced crosslinked polymer gel leakage plugging agent. J. Polym. Environ. 32 (11), 5677–5688. https://doi.org/10.1007/s10924-024-03334-1.

Cui, K., Jiang, G., Yang, L., et al., 2021. Preparation and properties of magnesium oxysulfate cement and its application as lost circulation materials. Pet. Sci. 18 (5), 1492–1506. https://doi.org/10.1016/j.petsci.2021.08.002.

Dai, L., Sun, J., Lv, K., et al., 2025. Cellulose nanofiber-reinforced supramolecular polymer gels for temporary plugging of fractured oil and gas reservoirs. Carbohydr. Polym. 356, 123370. https://doi.org/10.1016/j.carbpol.2025.123370.

ElTatawy, R.A., Ismail, A.M., Ayoup, M.S., et al., 2024. Preparation and kinetic studies of a new antibacterial sodium alginate gelatin hydrogel composite. Sci. Rep. 14 (1), 29206. https://doi.org/10.1038/s41598-024-80453-8.

Gao, K., Yang, Y., Yan, Q., et al., 2024. Preparation and study of a sodium alginate film for preventing spontaneous combustion of water-soaked coal in goaf. Energy 289, 130082. https://doi.org/10.1016/j.energy.2023.130082.

Guo, C., Jiang, G., Guan, J., et al., 2024a. Preparation and performance evaluation of a thixotropic polymer gel for loss circulation control. Fuel 371, 132148. https://doi.org/10.1016/j.fuel.2024.132148.

Guo, P., Qiu, Z., Zang, X., et al., 2024b. Epoxy resin microencapsulated by complex coacervation as physical-chemical synergetic lost circulation control material. Energy 293, 130630. https://doi.org/10.1016/j.energy.2024.130630.

Hamza, A., Shamlooh, M., Hussein, I.A., et al., 2020. Rheology of triamine functionalized silica reinforced polymeric gels developed for conformance control applications. Energy & Fuels 34 (1), 1093–1098. https://doi.org/10.1021/acs.energyfuels.9b03625.

Hu, C., Lu, W., Mata, A., et al., 2021. Ions-induced gelation of alginate: Mechanisms and applications. Int. J. Biol. Macromol. 177, 578–588. https://doi.org/10.1016/j.ijbiomac.2021.02.086.

Ji, D., Park, J.M., Oh, M.S., et al., 2022. Superstrong, superstiff, and conductive alginate hydrogels. Nat. Commun. 13 (1), 3019. https://doi.org/10.1038/s41467-022-30691-z.

Kang, Z., Liu, Y., Jia, H., et al., 2024. Progress and prospects of in situ polymer gels for sealing operation in wellbore and near-well zone. Energy & Fuels 38 (5), 3539–3563. https://doi.org/10.1021/acs.energyfuels.3c04382.

Kibikas, W., Chang, C., Bauer, S.J., et al., 2024. Time-dependent thermal degradation of lost circulation materials in geothermal systems. Geothermics 121, 103038. https://doi.org/10.1016/j.geothermics.2024.103038.

Lin, C., Xu, Q., Han, L., et al., 2024. Fracture sealing performance of granular lost circulation materials at elevated temperature: A theoretical and coupled CFD-DEM simulation study. Pet. Sci. 21 (1), 567–581. https://doi.org/10.1016/j.petsci.2023.10.002.

Lin, X., Shi, J., Meng, G., et al., 2023. Sodium alginate hydrogel carrier with calcium carbonate as calcium source for ibuprofen release. Macromol. Chem. Phys. 224 (21), 2300195. https://doi.org/10.1002/macp.202300195.

Liu, H., Li, X., Pan, Z., et al., 2025a. Lignin-based plugging hydrogel with high-temperature resistance and adjustable gelation. Adv. Compos. Hybrid Mater. 8 (1), 111. https://doi.org/10.1007/s42114-024-01132-w.

Liu, P., Wang, M., Fu, Y., et al., 2025b. Preparation and performance of an environmental-friendly degradable semi-interpenetrating network temporary plugging agent for acidification. Petrol. Sci. Technol. 43 (5), 508–534. https://doi.org/10.1080/10916466.2024.2305337.

Liu, Z., Liu, Q., Lin, L., et al., 2024. Stepwise reinforcement strategy for guar gum/sodium alginate based films: Introduction of carboxylated cellulose nanofibers by different methods and further calcium ion crosslinking. Food Hydrocoll. 156, 110266. https://doi.org/10.1016/j.foodhyd.2024.110266.

Lu, X., Li, Y., Feng, W., et al., 2019. Self-healing hydroxypropyl guar gum/poly (acrylamide-co-3-acrylamidophenyl boronic acid) composite hydrogels with yield phenomenon based on dynamic PBA ester bonds and H-bond. Colloids Surf. A Physicochem. Eng. Asp. 561, 325–331. https://doi.org/10.1016/j.colsurfa.2018.10.071.

Ma, R., Dai, L., Sun, D., et al., 2024. Nanocellulose/scleroglucan-enhanced robust, heat-resistant composite hydrogels for oilfield water plugging. Carbohydr. Polym. 341, 122320. https://doi.org/10.1016/j.carbpol.2024.122320.

Ming, Y., Shi, Z., Zhao, Y., et al., 2025. Preparation and characterization of microcapsules using an acid-tolerant sanxan gum combined with sodium alginate/chitosan and their application in Lactobacillus plantarum delivery. Carbohydr. Polym. 361, 123638. https://doi.org/10.1016/j.carbpol.2025.123638.

Mirabbasi, S.M., Ameri, M.J., Alsaba, M., et al., 2022. The evolution of lost circulation prevention and mitigation based on wellbore strengthening theory: A review on experimental issues. J. Petrol. Sci. Eng. 211, 110149. https://doi.org/10.1016/j.petrol.2022.110149.

Norioka, C., Inamoto, Y., Hajime, C., et al., 2021. A universal method to easily design tough and stretchable hydrogels. NPG Asia Mater. 13 (1), 34. https://doi.org/10.1038/s41427-021-00302-2.

Pan, X., Li, J., Ma, N., et al., 2023. Bacterial cellulose hydrogel for sensors. Chem. Eng. J. 461, 142062. https://doi.org/10.1016/j.cej.2023.142062.

Pereira, F.C., Clinckspoor, K.J., Moreno, R.B.Z.L., 2022. Optimization of an in-situ polymerized and crosslinked hydrogel formulation for lost circulation control. J. Petrol. Sci. Eng. 208, 109687. https://doi.org/10.1016/j.petrol.2021.109687.

Qin, D., Gao, W., Zhang, S., et al., 2023. In situ composite of graphene oxide in polyacrylamide to enhance strength of hydrogel with polyethyleneimine as crosslinker. Geoenergy Sci. Eng. 231, 212304. https://doi.org/10.1016/j.geoen.2023.212304.

Shariatinia, Z., Jalali, A.M., 2018. Chitosan-based hydrogels: Preparation, properties and applications. Int. J. Biol. Macromol. 115, 194–220. https://doi.org/10.1016/j.ijbiomac.2018.04.034.

Song, T., Ahdaya, M., Zhai, Z., et al., 2023. Comprehensive evaluation of a novel re-crosslinkable preformed particle gel for the water management of reservoir with concentrated divalent ions. Fuel 331, 125974. https://doi.org/10.1016/j.fuel.2022.125974.

Su, C., Li, D., Wang, L., et al., 2023. Green double crosslinked starch-alginate hydrogel regulated by sustained calcium ion-gluconolactone release for human motion monitoring. Chem. Eng. J. 455, 140653. https://doi.org/10.1016/j.cej.2022.140653.

Sun, D., Yang, Y., Liu, Y., et al., 2023a. Strengthening the hydrogel for lost circulation control through in situ self-assembled nanocomposite networks. Energy & Fuels 37 (6), 4320–4330. https://doi.org/10.1021/acs.energyfuels.2c04071.

Sun, D., Yang, Y., Ma, W., et al., 2023b. Heat-resistant hydrogel for temporary plugging in high-temperature and high-pressure fractured reservoirs. ACS Appl. Polym. Mater. 5 (10), 7746–7754. https://doi.org/10.1021/acsapm.3c00901.

Sun, Z., Wang, S., Zhu, Q., et al., 2023c. Insights into polyacrylamide hydrogels used for oil and gas exploration: Gelation time, gel strength, and adhesion strength. Energy & Fuels 37 (24), 19548–19561. https://doi.org/10.1021/acs.energyfuels.3c04004.

Wang, H., Liu, J., Fan, X., et al., 2022. Fabrication, characterisation, and application of green crosslinked sodium alginate hydrogel films by natural crab-shell powders to achieve drug sustained release. Lebensm. Wiss. Technol. 171, 114147. https://doi.org/10.1016/j.lwt.2022.114147.

Wang, J., Huang, Y., Liu, B., et al., 2021a. Flexible and anti-freezing zinc-ion batteries using a guar-gum/sodium-alginate/ethylene-glycol hydrogel electrolyte. Energy Storage Mater. 41, 599–605. https://doi.org/10.1016/j.ensm.2021.06.034.
Wang, L., Zhang, H.J., Liu, X., et al., 2021b. A physically cross-linked sodium alginate–gelatin hydrogel with high mechanical strength. ACS Appl. Polym. Mater. 3 (6), 3197–3205. https://doi.org/10.1021/acsapm.1c00404.
Wang, N., Wang, B., Wan, Y., et al., 2023a. Alginate-based composites as novel soil conditioners for sustainable applications in agriculture: A critical review. J. Environ. Manag. 348, 119133. https://doi.org/10.1016/j.jenvman.2023.119133.
Wang, R., Wang, C., Long, Y., et al., 2023b. Preparation and investigation of self-healing gel for mitigating circulation loss. Advances in Geo-Energy Research 8 (2), 112–125. https://doi.org/10.46690/ager.2023.05.05.
Wei, Z., Wang, M., Li, Y., et al., 2022. Sodium alginate as an eco-friendly rheology modifier and salt-tolerant fluid loss additive in water-based drilling fluids. RSC Adv. 12 (46), 29852–29864. https://doi.org/10.1039/D2RA04448J.
Wei, Z., Wang, M., Shan, W., et al., 2024. Synergistic effects of potassium alginate and silicates co-inhibition performance in shale hydration. J. Mol. Liq. 393, 123538. https://doi.org/10.1016/j.molliq.2023.123538.
Wu, S., Lou, D., Wang, H., et al., 2022. One-pot synthesis of anti-freezing carrageenan/polyacrylamide double-network hydrogel electrolyte for low-temperature flexible supercapacitors. Chem. Eng. J. 435, 135057. https://doi.org/10.1016/j.cej.2022.135057.
Wu, Y., Yan, X., Huang, Y., et al., 2024. Ultra-deep reservoirs gel fracturing fluid with stepwise reinforcement network from supramolecular force to chemical cross-linking. Energy 293, 130632. https://doi.org/10.1016/j.energy.2024.130632.
Xie, B., Ma, J., Wang, Y., et al., 2021. Enhanced hydrophobically modified polyacrylamide gel for lost circulation treatment in high temperature drilling. J. Mol. Liq. 325, 115155. https://doi.org/10.1016/j.molliq.2020.115155.
Xie, F., 2024. Alginate-based nanocomposites for food preservation: Recent progress showcasing heightened material properties and functionalities. Advanced Nanocomposites 1 (1), 248–274. https://doi.org/10.1016/j.adna.2024.07.002.
Xu, C., Zhang, H., She, J., et al., 2023. Experimental study on fracture plugging effect of irregular-shaped lost circulation materials. Energy 276, 127544. https://doi.org/10.1016/j.energy.2023.127544.
Yan, X., Huo, B., Deng, S., et al., 2024. The role of physical lost circulation materials type on the evolution of strong force chains of plugging zone in deep fractured tight reservoir. Powder Technol. 432, 119149. https://doi.org/10.1016/j.powtec.2023.119149.
Yang, H., Iqbal, M.W., Lashari, Z.A., et al., 2019. Experimental research on amphiphilic polymer/organic chromium gel for high salinity reservoirs. Colloids Surf. A Physicochem. Eng. Asp. 582, 123900. https://doi.org/10.1016/j.colsurfa.2019.123900.
Yang, L., Xie, C., Ao, T., et al., 2022. Comprehensive evaluation of self-healing polyampholyte gel particles for the severe leakoff control of drilling fluids. J. Petrol. Sci. Eng. 212, 110249. https://doi.org/10.1016/j.petrol.2022.110249.
Yin, Z., Wang, Y., Wang, K., et al., 2018. The adsorption behavior of hydroxypropyl guar gum onto quartz sand. J. Mol. Liq. 258, 10–17. https://doi.org/10.1016/j.molliq.2018.02.105.
Zang, X., Qiu, Z., Guo, P., et al., 2025. Development and performance evaluation of a mechanically triggered release microcapsule based on in-situ polymerization for lost circulation control. Colloids Surf. A Physicochem. Eng. Asp. 705, 135720. https://doi.org/10.1016/j.colsurfa.2024.135720.
Zhai, K., Yi, H., Liu, Y., et al., 2020. Experimental evaluation of the shielded temporary plugging system composed of calcium carbonate and acid-soluble preformed particle gels (ASPPG) for petroleum drilling. Energy & Fuels 34 (11), 14023–14033. https://doi.org/10.1021/acs.energyfuels.0c02810.
Zhang, H., Song, Q., Deng, Z., et al., 2024. Sodium alginate hydrogel toughened by guar gum for strain sensors. Polym. Bull. 81 (9), 8045–8056. https://doi.org/10.1007/s00289-023-05075-y.
Zhang, X., Deng, J., Yang, K., et al., 2022. High-strength and self-degradable sodium alginate/polyacrylamide preformed particle gels for conformance control to enhance oil recovery. Pet. Sci. 19 (6), 3149–3158. https://doi.org/10.1016/j.petsci.2022.06.012.
Zhao, L., Yuan, C., Shan, K., et al., 2025a. Expandable profile liner technology for mitigating lost circulation and wellbore instability in geothermal drilling. Renew. Sustain. Energy Rev. 209, 115109. https://doi.org/10.1016/j.rser.2024.115109.
Zhao, X., Wang, W., Cheng, B., et al., 2025b. Preparation of TEMPO-partially oxidized sodium alginate/SF scaffolds with degradation compatibility for skin defect repair. Carbohydr. Polym. 357, 123437. https://doi.org/10.1016/j.carbpol.2025.123437.